



HAL
open science

Validation of 4D flow based relative pressure maps in aortic flows

David Nolte, Jesús Urbina, Julio Sotelo, Leo Sok, Cristian Montalba, Israel Valverde, Axel Osses, Sergio Uribe, Cristobal Bertoglio

► **To cite this version:**

David Nolte, Jesús Urbina, Julio Sotelo, Leo Sok, Cristian Montalba, et al.. Validation of 4D flow based relative pressure maps in aortic flows. 2020. hal-02113750v3

HAL Id: hal-02113750

<https://hal.science/hal-02113750v3>

Preprint submitted on 28 Oct 2020

HAL is a multi-disciplinary open access archive for the deposit and dissemination of scientific research documents, whether they are published or not. The documents may come from teaching and research institutions in France or abroad, or from public or private research centers.

L'archive ouverte pluridisciplinaire **HAL**, est destinée au dépôt et à la diffusion de documents scientifiques de niveau recherche, publiés ou non, émanant des établissements d'enseignement et de recherche français ou étrangers, des laboratoires publics ou privés.

Validation of 4D Flow based relative pressure maps in aortic flows

David Nolte^{a,b}, Jesús Urbina^{c,d,e}, Julio Sotelo^{c,e,f,g}, Leo Sok^a, Cristian Montalba^{c,e}, Israel Valverde^h, Axel Osses^{b,e}, Sergio Uribe^{c,d,e}, Cristóbal Bertoglio^{a,b}

^a*Bernoulli Institute, University of Groningen, Groningen, 9747AG, The Netherlands*

^b*Center for Mathematical Modeling, Universidad de Chile, Santiago, 8370456, Chile*

^c*Biomedical Imaging Center, Pontificia Universidad Católica de Chile, Santiago, 7820436, Chile*

^d*Department of Radiology, School of Medicine, Pontificia Universidad Católica de Chile, Santiago, 833002, Chile*

^e*Millennium Nucleus for Cardiovascular Magnetic Resonance, Santiago, 7820436, Chile*

^f*School of Biomedical Engineering, Universidad de Valparaíso, Valparaíso, Chile*

^g*Department of Electrical Engineering, Pontificia Universidad Católica de Chile, Santiago, 7820436, Chile*

^h*Hospital Universitario Virgen del Rocío, Sevilla, 41013, Spain*

Abstract

While the clinical gold standard for pressure difference measurements is invasive catheterization, 4D Flow MRI is a promising tool for enabling a non-invasive quantification, by linking highly spatially resolved velocity measurements with pressure differences via the incompressible Navier–Stokes equations. In this work we provide a validation and comparison with phantom and clinical patient data of pressure difference maps estimators.

We compare the classical Pressure Poisson Estimator (PPE) and the new Stokes Estimator (STE) against catheter pressure measurements under a variety of stenosis severities and flow intensities. Since it is the clinical range of interest and Reynolds stress measurements in 4D Flow MRI are only feasible in controlled experimental settings, we perform the validation on standard clinical 4D Flow data, and therefore on laminar flows and pressure gradients. However, we also show the limits of such methods on transitional flow. Specifically, we use several 4D Flow data sets of realistic aortic phantoms with different anatomic and hemodynamic severities and two patients with aortic coarctation.

In all cases, the STE method yields more accurate results than the PPE method compared to catheterization data. The results indicate an improved robustness of the STE method with respect to variation in lumen segmentation. The superiority of the STE becomes more evident when increasing the Reynolds

*Correspondence to: Cristóbal Bertoglio, Bernoulli Institute, University of Groningen, Groningen, 9747AG, The Netherlands

Email address: c.a.bertoglio@rug.nl (Cristóbal Bertoglio)

number, hence being able to better capture pressure gradients when moving to transitional flow regimes.

Keywords: 4D Flow, pressure difference, catheter, clinical and experimental validation

1. Introduction

Aortic coarctation (AoCo) is a narrowing of the proximal descending aorta (DAo), typically located at the level of the aortic isthmus. AoCo accounts for 5–8% of all congenital heart defects (CHD) and the prevalence of isolated forms is 3 per 10000 live births [1]. The peak-to-peak pressure difference across the AoCo is the most important hemodynamic parameter for clinical decisions [2, 3].

In the clinical practice, different techniques are available to measure pressure differences across AoCo's. Catheterization is the gold standard technique, but is expensive, invasive, non-exempt of risk, the patient is exposed to X-rays and is difficult to reproduce. Doppler echocardiography using the simplified Bernoulli equation is the most available non-invasive method, but has certain limitations: it is operator dependent, has poor acoustic windows and spectral broadening, and in addition overestimates the peak velocities by up to 25% [4]. Magnetic resonance imaging (MRI) is able to obtain images of the heart and the great vessels, with coverage of the entire cardiovascular system, for the assessment of the anatomy, function and flow. The MRI procedure to measure three-dimensional and time-dependent flow, referred to as 3D cine phase contrast MRI or 4D Flow, consists in the acquisition of an anatomical image and velocity-encoded images in three orthogonal directions [5, 6]. 4D Flow allows to measure non-invasively the 3D-spatial and temporal evolution of complex flow patterns, enabling the quantification of different hemodynamic parameters [7].

In particular, 4D Flow allows to infer pressure maps using the Navier–Stokes equations along the thoracic aorta.

In order to obtain those maps, the classical method is solving a Pressure Poisson Estimator (PPE) by taking the divergence of the Navier–Stokes equations and inserting the velocity measurements in the right-hand-side [8, 9]. More recently, several additional methods have been introduced, see [10] for a comprehensive review. In particular, the Stokes Estimator (STE) [11] computes 3D pressure maps using a Stokes equation based on the physical pressure and an auxiliary, non-physical velocity field.

In addition to PPE and STE, less computationally expensive methods exist, like the Work Energy-derived Relative Pressure (WERP) method [12] based on an integral energy balance of the Navier–Stokes equation, the integral momentum relative pressure estimator (IMRP) [10] based on integral linear momentum conservation, or the virtual WERP (*v*WERP) method [13] based on a different treatment of the convective term than in the IMRP. Using numerical data, the WERP has shown better accuracy than the PPE, but worse accuracy than the STE and IMRP, while the two latter were shown to have similar accuracy [10].

The v WERP method was reported to be more versatile, accurate and robust
 40 than the PPE and the WERP methods [13], but has not been compared to STE
 or IMRP. A particular limitation of WERP is the assumption that the studied
 vessel segment does not include any bifurcations. As a consequence, the method
 cannot be used to estimate the pressure difference between the ascending aorta
 (AAo) and the DAo due to the presence of the supra-aortic branches. More-
 45 over, instead of 3D relative pressure maps, WERP, IMRP and v WERP can only
 deliver mean pressure differences between two planes of the vessel of interest.
 They are therefore difficult to apply in cases when pressure spatial variations
 are present as in post stenotic areas. For all the aforementioned reasons, in this
 work we consider only the PPE and the STE methods.

50 Several validation studies were carried out for the PPE method [14, 15, 16].
 An in vitro validation study showed a good correlation between PPE and
 catheter pressure differences ($r = 0.89$, $p < 0.001$) in the simple setting of
 an elastic straight tube phantom [14]. The PPE method was further assessed
 in 13 patients with moderate AoCo in [15], where instantaneous peak pressure
 55 differences from 4D Flow were found to be slightly underestimated on average
 in comparison to the catheterization data, with a bias of 1.5 mmHg and a vari-
 ability of ± 4.6 mmHg (two standard deviations). Also in [16], PPE pressure dif-
 ferences showed good agreement with catheter measurements in AoCo patients
 in cases with sufficient spatial image resolution (at least 5 voxels/diameter).
 60 However, systematic underestimation of the pressure difference was found for
 lower resolutions (3.4 ± 0.64 voxels/diameter).

To the best of the authors' knowledge, no validation studies have been
 reported for the STE method using experimental or patients' 4D Flow and
 catheterization data. The aim of this work is therefore to fill this gap and study
 65 the effects of the MR image resolution and aortic segmentation, cardiac out-
 put and severity of the AoCo on the accuracy of both PPE and STE methods
 from 4D Flow and catheterization data. This is achieved by using data from
 a realistic MRI compatible AoCo phantom that the authors have designed and
 studied [17]. We have also included the comparison of these methodologies in 2
 70 patients. The present study is the first reported validation of the STE method
 using measured data.

2. Theory

2.1. Problem statement

Maps of relative pressure can be computed directly from the velocity mea-
 surements by evaluating the linear momentum conservation equation of the
 incompressible Navier–Stokes model, i.e.,

$$\rho \frac{\partial \vec{u}}{\partial t} + \rho(\vec{u} \cdot \nabla)\vec{u} = -\nabla p + \mu \Delta \vec{u} \quad (1)$$

where ρ is the density of the fluid and μ its dynamic viscosity, $\vec{u} : \Omega \times [0, T] \mapsto \mathbb{R}^3$
 75 denotes the velocity vector field (to be obtained by means of 4D Flow) and

$p : \Omega \times [0, T] \mapsto \mathbb{R}$ is the pressure field. Ω represents the computational domain obtained from segmenting the 4D Flow images (see section 3.3 and Fig. 2), its boundary—corresponding to the vessel wall—is denoted $\partial\Omega$. The considered time interval $[0, T]$ represents one cardiac cycle.

In the case of turbulent flows, the velocity can be considered as a superposition of a temporal or ensemble average, \vec{u} , and stochastically fluctuating, turbulent contributions, \vec{u}' . Using the decomposition $\vec{u} = \vec{u} + \vec{u}'$ in (1) and ensemble-averaging yields the Reynolds-averaged Navier–Stokes (RANS) equations [18],

$$\rho \frac{\partial \vec{u}}{\partial t} + \rho(\vec{u} \cdot \nabla)\vec{u} = -\nabla \bar{p} + \mu \Delta \vec{u} - \rho \nabla \cdot \overline{\vec{u}' \otimes \vec{u}'}. \quad (2)$$

80 The last term is the so-called Reynolds stress tensor and represents the effect of turbulent fluctuations on the averaged velocity field, \vec{u} . If the flow is laminar (non-turbulent), $\vec{u}' = \vec{0}$, $\vec{u} = \vec{u}$, $\bar{p} = p$, and (1) and (2) are identical.

4D Flow velocity fields can be considered as measurements of \vec{u} since the images are assembled from the ensemble of many repeated signal acquisitions
85 during finite temporal windows [7], merging in every time-resolved image information from many instants of time, which results in smoothing [19]. However, the evaluation of the last term in Eq. (2) requires measurements of the velocity fluctuations or the Reynolds stress tensor directly. Recently, extended Flow MRI sequences have been presented that enable measuring the full Reynolds stress
90 tensor, e.g., the ICOSA6 sequence [20], involving 6 motion encoding directions and leading to vastly increased scan times.

Flow through clinically borderline stenoses are mostly in laminar, sometimes transitional regimes. Therefore, optimizing the accuracy of pressure gradients estimators in the laminar regime is of great importance for the clinical trans-
95 lation of such methods. The goal of this work is hence to assess the accuracy of laminar 4D Flow based relative pressure estimators (i.e., neglecting the last term of Eq. (2)) using current clinically available 4D Flow data.

Relative pressure maps are reconstructed from 4D Flow data by means of the Pressure Poisson Estimator (PPE) approach [8, 21, 9] and the Stokes Estimator
100 method (STE) [11, 22], which will be described in this section.

Discretizing Eq. (1) in time, here with the first order backward difference formula, gives the following expression for the pressure gradient:

$$-\nabla p^k = \rho \frac{\vec{u}^k - \vec{u}^{k-1}}{\Delta t} + \rho(\vec{u}^k \cdot \nabla)\vec{u}^k - \mu \Delta \vec{u}^k. \quad (3)$$

The indices $1 \leq k \leq N$ denote the time snapshot of the measurements and Δt the temporal offset between two consecutive measurements or cardiac phases, with time stamps $t_k = k\Delta t$. For the first step, $k = 1$, a forward difference has to be used instead since no previous measurements are available. Evaluating the right hand side of Eq. (3) for spatially undersampled and noisy velocity measurements \vec{u}_m ,

$$R^k := \rho \frac{\vec{u}_m^k - \vec{u}_m^{k-1}}{\Delta t} + \rho(\vec{u}_m^k \cdot \nabla)\vec{u}_m^k - \mu \Delta \vec{u}_m^k. \quad (4)$$

yields a pressure estimate from its approximate gradient $\nabla \hat{p}^k \approx \nabla p^k$, given by

$$-\nabla \hat{p}^k = R^k. \quad (5)$$

Higher order time schemes, while more accurate in theory for small time steps, are not beneficial in the present context due to the coarse time sampling of the measured velocities. Note that in previous works, for instance in [10, 13] a second-order mid-point scheme was used. However, this leads to stronger
105 underestimations of the pressure differences. This can be explained from the nature of time under-sampling in MRI, namely that u_m^k is reconstructed by assuming the flow velocity as constant within the interval $[t^k - \Delta t/2, t^k + \Delta t/2]$ rather than being an instantaneous measurement at t^k [7].

It is important to remark that in all methods derived from the Navier–Stokes
110 equations, e.g., Bernoulli-based, PPE, STE, and in CFD simulations, at any instant of time, the pressure is uniquely defined up to a constant (with respect to the spatial coordinates). Therefore, only instantaneous pressure differences between different locations can be compared at different times. Catheterization or sphygmomanometer pressure measurements are taken relative to the
115 atmospheric pressure. Hence, the pressures are calibrated with respect to a global reference and pressure values can be compared at different times and among patients. A common measure in the clinical practice are the so-called peak-to-peak pressure differences, which compares the largest pressure difference registered between two locations at any time during the cardiac cycle, thus
120 taking into account time shifts due to the vessel elasticity. Peak-to-peak pressure differences can only be determined by means of catheterization or with the models described above when calibrated with catheterization data, which however violates the non-invasiveness of the estimation methods. For this reason, the present work focuses on instantaneous pressure differences instead of
125 peak-to-peak values.

Based on Eq. (5), the Pressure Poisson Estimator (PPE) and the Stokes Estimator (STE) method will be described next.

2.2. Pressure Poisson Estimator (PPE)

Assuming sufficient regularity (i.e., assuming that all required derivatives exist), a Poisson equation for the pressure estimation can be obtained by taking the divergence of (5),

$$-\Delta \hat{p}^k = \nabla \cdot R^k. \quad (6)$$

Solving Eq. (6) requires boundary conditions (BCs) on the entire boundary surface $\partial\Omega$ of the computational domain Ω . A priori, no physical BCs for the pressure are known. An artificial Neumann BC can be obtained by projection of Eq. (5), restricted to $\partial\Omega$, to the outward unit normal vector on the wall, \vec{n} ,

$$\vec{n} \cdot \nabla \hat{p}^k = \vec{n} \cdot R^k. \quad (7)$$

Eq. (6) with BCs (7) can be discretized in space with the finite element method
130 (FEM). In order to ensure that the resulting algebraic problem admits a unique solution, the pressure can be fixed arbitrarily at one point of the mesh via a Dirichlet boundary condition, without changing the pressure gradient.

2.3. Stokes Estimator (STE)

The Stokes Estimator introduces a divergence-free auxiliary function \vec{w} with $\vec{w} = \vec{0}$ on $\partial\Omega$. The Laplacian of \vec{w} is subtracted from Eq. (5) as a regularization term (with unitary viscosity here for simplicity) and we obtain

$$\begin{aligned} -\Delta\vec{w} - \nabla\hat{p}^k &= R^k & \text{in } \Omega \\ \nabla \cdot \vec{w} &= 0 & \text{in } \Omega \\ \vec{w} &= \vec{0} & \text{on } \partial\Omega. \end{aligned} \tag{8}$$

The auxiliary function \vec{w} holds no physical interest, and it is expected to be negligible compared to the pressure term as long as the right-hand-side R^k is the gradient of a scalar (irrotational). The advantages of the STE with respect to the PPE method are (1) that no artificial BCs for the pressure are necessary and (2) that it has lower regularity requirements, since no additional derivatives are applied on the measurements R^k . In fact, in contrast to the PPE method, the STE method searches the pressure in the natural energy space of the pressure in the original Navier–Stokes equations [23]. As for the PPE method, the pressure constant has to be fixed for ensuring solvability of the algebraic problem.

3. Materials and methods

3.1. Aortic Phantom Study

3.1.1. Phantom setup

The experimental setup of the aortic phantom study is described in detail in [17] and [24]. The phantom represents the thoracic aortic circulation with a closed circuit, consisting in a MR-compatible pulsatile unit pump with a control unit (CardioFlow 5000 MR, Shelley Medical Imaging Technologies, London, Canada) and a realistic aortic model built with flexible silicone (T-S-N 005, Elastrat, Geneva, Switzerland). The control unit was configured to simulate two physiological aortic flow conditions—rest conditions at 75 bpm and stress conditions at 136 bpm—, calibrated with average data of ten healthy volunteers.

The resulting peak flow in the AAO was 4.5 mL/min under rest conditions and 5.9 mL/min under stress conditions.

These flow conditions correspond to peak Reynolds numbers $Re = \rho UD/\mu$ at the inlet of $Re \sim 3500$ at rest and $Re \sim 5000$ under stress conditions, at the time corresponding to peak systole. Re is based on the diameter of the inlet tube D (as recovered from the 4D Flow images) and the average velocity U over a cross-section upstream of the aortic phantom.

Different degrees of AoCo were placed in the DAo just after the left subclavian artery (at the isthmus level). AoCo’s were built with Technyl with an effective orifice of 13 mm, 11 mm and 9 mm and a length of 10 mm, leading to degrees of stenosis of 40 %, 50 % and 60 % with respect to the native DAo distal to the AoCo. The liquid used in the system consisted of a homemade volume-mixing blood mimicking fluid with 60 % distilled water and 40 % glycerol (Orica Chemicals, Watkins, CO), with a density of 1.119 g/cm³, viscosity

of 4.83×10^{-3} Pa s [25, 26], and a T1 value of 900 ms, which are representative values for human blood. The density and viscosity values of the mixture were confirmed using an empirical formula reported by [27] with an ambient temperature of 22 °C.

3.1.2. Catheterization

The phantom was equipped with a catheterization unit to measure invasively and simultaneously the pressure gradient across the AoCo. For this purpose, two catheters (5 French, Soft-Vu, AngioDynamics, Latham, NY) of side-hole type with transducers (AngioDynamics) were placed in the AAo and 2 cm after the AoCo and were connected to a patient monitor (Contec Medical Systems, Hebei, China). The pressure catheters were zeroed at the same height of the phantom.

Pressure information from the two catheters was recorded simultaneously during 1 minute in the AoCo phantoms (40 %, 50 % and 60 % degrees of stenosis) at rest and at stress conditions, using the commercial software Central Monitor System V3.0 (Contec Medical System). The pressure difference is obtained by subtracting the averages of both signals over the cardiac cycles. The average cycle (the so-called phase average) was obtained by first upsampling and filtering the signals, then determining the instantaneous phase angles by means of applying the Hilbert transform [28] to the band-pass filtered signal around the cardiac rate. The phase angle interval $]-\pi, \pi]$ was split into 52 (rest) or 28 (stress) segments, and the original signal was associated to these segments according to the instantaneous phase angles. The phase averages and phase standard deviations were found by averaging (or computing the standard deviation) within each phase segment. The phase-averaged pressure signals and the corresponding phase variabilities are illustrated in Figs. A.10. At the peak time, the value of two phase standard deviations, 2σ (95.45 % confidence interval), ranges between 10 mmHg (40 % at rest) and 27 mmHg (40 % at stress). For the pressure difference, 2σ lies in the interval $[0.8, 11]$ mmHg.

3.1.3. 4D Flow data acquisition

Phantom data were acquired in a 1.5 T MRI system (Achieva, Philips, The Netherlands) using a 4-channel body coil and retrospective cardiac gating. The control unit of the pulsatile pump generated a trigger signal to synchronize the MR data acquisition. In order to provide static tissue for phase correction algorithms used in PC-MRI, 6 L of 1 % agar were placed around the aortic phantom at least 6 hours before scanning.

4D Flow images were acquired with an isotropic voxel size of 0.9 mm for all phantoms (AoCo with 40 %, 50 % and 60 % degrees of stenosis) under rest and stress conditions. In order to study the effect of image resolution of the pressure gradient estimation procedure, different synthetic low resolution data (1.4 mm and 2.0 mm isotropic voxel) were generated from the original image (0.9 mm isotropic voxel) using linear interpolation. The acquisition parameters are summarized in Tab. 1 (see column “in-vitro experiments”).

A detailed discussion of the dominant flow features in the 4D Flow data is included in Appendix A.2.

3.2. Patient study: 4D-Flow MRI and catheterization

In addition to the phantom study, we include two subjects with AoCo (*Subject 1*: 12 years, weight 47 kg, height 151 cm; *Subject 2*: 35 years, weight 63 kg, height 205 cm). Subject 1 presented a native AoCo and mild aortic valve stenosis, mild left ventricular hypertrophy and systemic hypertension at rest. Subject 2 presented a repaired AoCo using a subclavian flap. In addition, there was a very mild narrowing at the level of the transverse arch, close to the isthmus and a mild dilatation in the proximal DAo. Angiographic contrast agent enhanced images of the patients' aortas with anatomical information and 4D Flow streamlines are displayed in Fig. A.13. The cardiac output obtained from the 4D Flow data for Subjects 1 and 2 were 3.27 L/min and 6.49 L/min, respectively.

The clinical patient data were acquired in a combined MRI/Catheter interventional suite (XMR, see [29] for a more detailed description), equipped with a 1.5 T Achieva MR scanner and a BT Pulsera cardiac radiography unit (Philips, Best, Netherlands) [30, 31]. Patients had general anesthesia according to institutional protocol. Two femoral artery vascular accesses by percutaneous puncture were performed. A heparin bolus of 50 IU/Kg was given with activated clotting time monitoring once vascular access was obtained. A MRI compatible multi-purpose catheter was advanced under fluoroscopic guidance from the right femoral artery to the AAo just above the aortic sinus for continuous hemodynamic pressure monitoring. A second multi-purpose catheter in the left femoral artery was advanced to the abdominal aorta at the level of the diaphragm. The catheter positions are visually determined during the fluoroscopy procedure by the interventionist. We used these positions in the 4D Flow based pressure computation as shown in Fig. A.13. The floating table was then moved to transfer the patient to the MRI scan to acquire the 4D Flow MRI data. Following the acquisition of the MR data the patient was transferred back to the catheter table. Catheter pullbacks were performed using a biplane system (Siemens Axiom-Artis d-TA, Siemens, Germany) for evaluating the pressure distribution along the aorta. X-rays images were acquired with a frame rate of 15 images per second.

Phase-averaging of the catheter pressure signals was achieved by identifying and splitting the cardiac cycles according to the pressure peak locations and subsequent averaging over the resampled cycles.

The data was acquired at St. Thomas' Hospital, London, UK. The local research ethics committee approved this retrospective study and informed consent was obtained from all patients.

Tab. 1 summarizes the acquisition parameters for the in-vivo study (see column "in-vivo experiments").

3.3. Segmentation and mesh generation

The 4D Flow data sets were processed using an in-house MATLAB library (The MathWorks, Natick, MA), similarly to previous studies [32, 33]. The

Table 1: MR acquisition parameters

| | in-vitro experiments | in-vivo experiments |
|----------------------|-----------------------------------|-----------------------------|
| FOV (mm) | $200 \times 200 \times 114$ | $270 \times 270 \times 125$ |
| Matrix size | $224 \times 224 \times 127$ | $144 \times 144 \times 50$ |
| Recon. voxel (mm) | $0.9 \times 0.9 \times 0.9$ | $1.9 \times 1.9 \times 2.5$ |
| TFE factor | rest: 2, stress: 1 | rest: 2 |
| Cardiac phases | 25 | 28 |
| Time resolution (ms) | rest: 32, stress: 18 | rest: 26 |
| VENC (cm/s) | rest: 160–400, stress: 250–500 | rest: 300 |
| TE/TR (ms) | 3.7/6.4 | 2.4/3.8 |
| Flip angle (deg) | 6.5 | 5 |
| Scan time (min) | 18–22 | 19 |

255 library contains a homemade segmentation toolbox, which consists in (a) a contrast adjustment of the images to increase the intensities in the vessel of interest, prior to (b) performing a 3D threshold and 3D labeling of the different regions of interest in the images. If the user agrees with the selected thresholding level, the next step (c) is the iterative manual disconnection of different objects
260 inside the image. 3D labeling at this step is used to verify that the disconnection was performed properly.

The segmentation procedure of the patient’s data used the angiographic image, i.e., the time average of the anatomic images multiplied by the magnitude of the velocities images, as described in [34]. For the phantom data, the good
265 contrast between the lumen of the vessel and the agar-agar used in the phantom reservoir enabled the segmentation based on the time average of the anatomic images. Fig. 1 illustrates the procedure.

The toolchain proceeds as illustrated in Fig. 2. Structured tetrahedral meshes (Fig. 2(b)) were created from the segmented images, such that the mesh
270 vertices matched the centers of the image voxels. The velocity vectors attributed to each voxel of the 4D Flow images were transferred to the corresponding mesh vertices (Fig. 2(c)). The last step in the toolchain consisted in the pressure map reconstruction (Fig. 2(d)), described in the next section.

In order to study the effect of different segmentations on the pressure difference estimates, additional segmentations were created for the phantom velocity
275 images at 0.9 mm voxel size. A reference segmentation was modified by adding or subtracting one voxel at the boundary, thus extending or decreasing the lumen cross-section.

For the patient data, only the original segmentations obtained with the procedure described above were used, since the large voxel size of 2 mm with respect
280 to the aortic diameter did not allow eliminating boundary voxels in one of the patients.

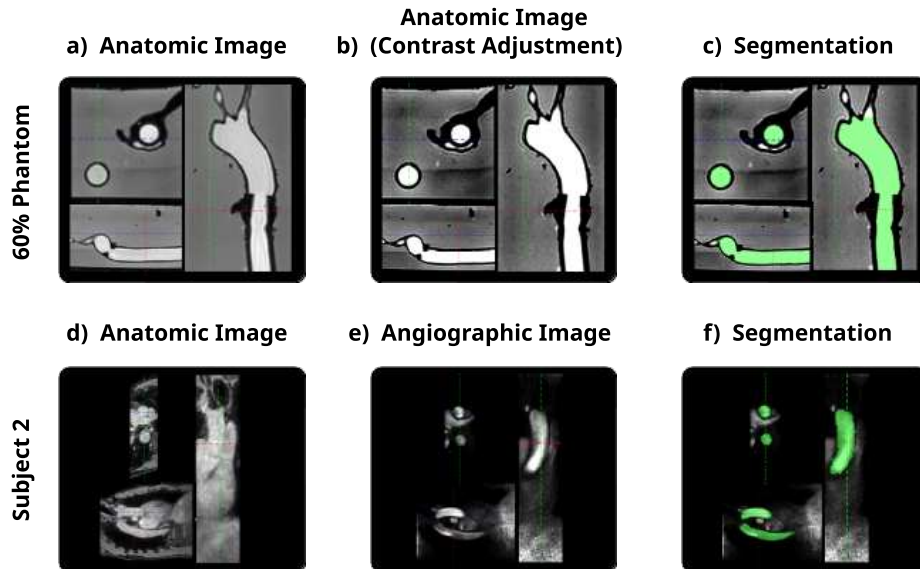


Figure 1: Segmentation procedure. Phantom data (first row, 60 % degree of stenosis example): (a) anatomic images (left column) are enhanced by contrast adjustment (middle column), before (b) applying a 3D threshold and region labeling and (c) iteratively performing manual disconnection of different objects present in the image for each slice, to yield the final segmentation (right column). Patient data (second row): instead of a contrast adjusted anatomic image, step (a) produces an angiographic image, steps (b) and (c) as for phantom data.

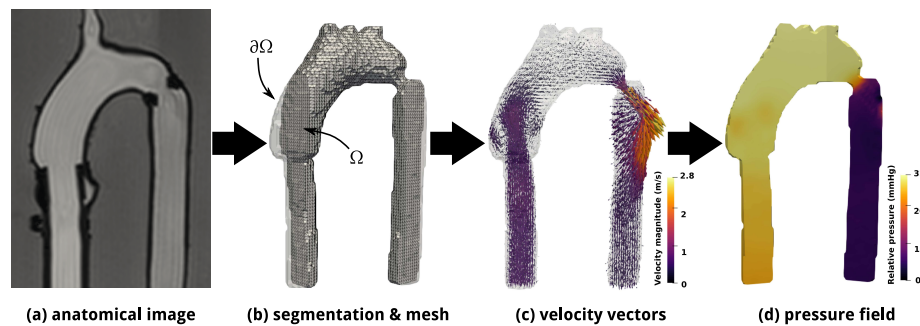


Figure 2: Pressure recovery toolchain. (a) 2D section from the anatomic image of 4D Flow, (b) structured tetrahedral mesh (grey, cropped) from segmentation (transparent) of the anatomical image, corresponding to the computational domain Ω and its boundary $\partial\Omega$, (c) representation of 4D Flow velocity vectors on mesh, (d) pressure maps from velocity data (cuts through centers of AAo and DAo). Example data of the 60 % AoCo phantom at rest, at time of peak systole.

3.4. Pressure maps computation

Pressure maps were computed from all 4D Flow data sets with the PPE and
285 STE methods. The pressure differences, to be compared with the corresponding
catheter values, were defined as differences of the pressure averages over two
spheres with a radius of 4 mm at locations proximally and distally to the AoCo.
Averaging over several voxels rendered the pressure estimate more robust to
local perturbations, e.g., induced by noise in the 4D Flow data.

290 The corresponding partial differential equations of the PPE and STE meth-
ods were discretized with the finite element method (FEM). Velocity measure-
ments were assumed to be piece-wise linear (\mathbb{P}^1) finite element functions on the
tetrahedral meshes described in the previous section. Linear \mathbb{P}^1 elements were
also used to discretize the PPE and the STE systems, Eq. (6) and Eq. (8). In the
295 latter case, standard pressure stabilization (Brezzi–Pitkaranta) was employed to
ensure the solvability of the saddlepoint problem, avoiding the requirement of
higher order elements.

The code was implemented using the FEM library FEniCS [35]. The re-
sulting algebraic linear system of the STE problem was four times larger than
300 that of the PPE method, resulting in higher memory requirements and compu-
tational times. Direct solvers were used for solving the linear systems, taking
advantage of re-using the LU factorization of the system matrix at the first
time-step for all subsequent steps.

The results presented in this article were computed on a standard desktop
305 computer with 32 GB RAM and an Intel i7-4790K CPU.

4. Results

4.1. Phantom study

The relative pressure fields at peak systole obtained with the STE method
are illustrated in Fig. 3 along two cuts through the center of the DAo and
310 AoCo, and through the AAo, for all AoCo phantoms under rest and stress
conditions. The small spheres indicate the volumes over which the pressure
is averaged for the computation of the pressure differences. In all cases, the
AoCos produce strong pressure gradients across the constrictions. The AAo–
DAo pressure differences increase with AoCo severity and are higher under stress
315 than under rest conditions. Local pressure minima are present in the AAo, close
to the exit of the inlet tube, associated to recirculating flow. For all cases a
relatively higher pressure can be appreciated at the DAo location where the jet
produced by the AoCo impinges the wall. In the 60 % stress case, small scale
wiggles with high amplitude appear downstream of the AoCo.

320 Fig. 4 compares the maximum instantaneous pressure differences obtained
with the PPE and the STE methods with catheterization data for all investi-
gated phantoms.

The figure presents the data obtained with the three image resolutions,
0.9 mm, 1.4 mm and 2 mm, in separate plots. Each plot shows the STE (left
325 column) or PPE results (right column) obtained using the three segmentations,

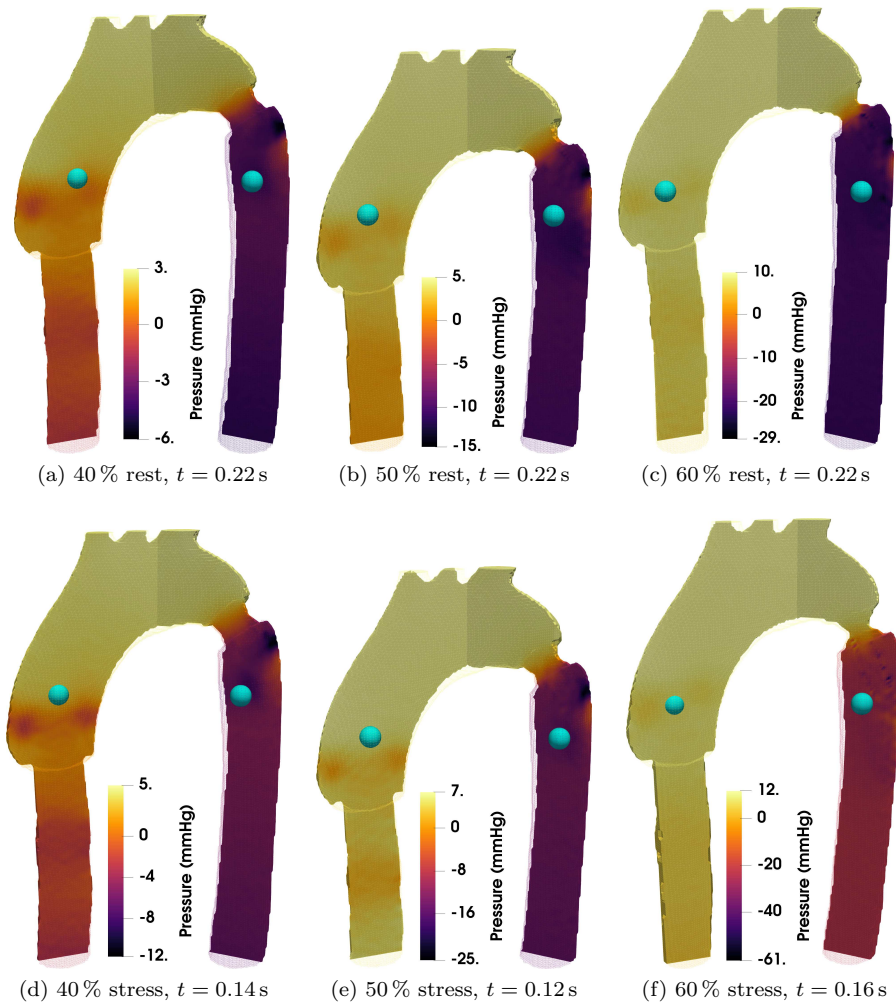


Figure 3: Pressure fields obtained with the STE method, using the standard segmentation V+0 at a voxel size of 0.9 mm, for all AoCo severities under rest and stress conditions, at the time of the observed peak pressure difference.

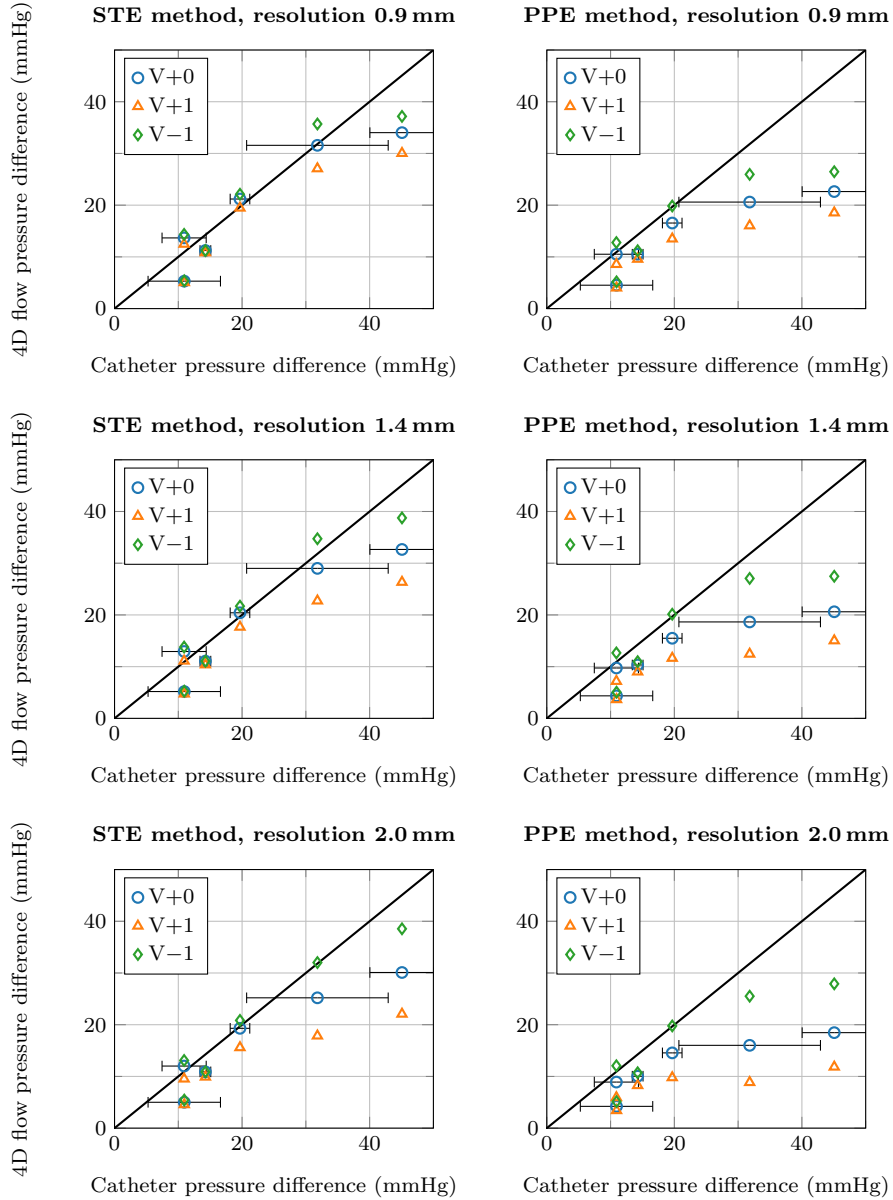


Figure 4: Comparison of 4D Flow peak pressure differences obtained with the STE (left column) and the PPE (right column) methods with respect to catheterization, for all in-vitro severities (AoCo with degrees of stenosis of 40%, 50% and 60% at rest and stress). V+0 refers to a reference segmentation; the segmentation V+1 extends V+0 by 1 voxel in each direction, in V-1 the outer layer of voxels of V+0 is deleted. Top row: results obtained for 0.9 mm voxel size; middle row: 1.4 mm voxel size; bottom row: 2 mm voxel size.

denoted V+0 (initial segmentation), V−1 (outermost layer of voxels eliminated along the boundary) and V+1 (1 layer of voxels added at the boundary), for all investigated scenarios. The diagonal line indicates perfect correspondence of 4D Flow and catheter pressure differences. The horizontal error bars attached to the V+0 markers indicate two standard deviations (i.e., the 95.45 % confidence interval) of the catheter pressure differences (the phase-averaged pressure signals and their associated uncertainties are shown in Fig. A.10).

A strong dependence on the segmentation exists particularly for pressure differences above 30 mmHg and is more pronounced for large voxel sizes. The PPE results are also more sensitive to the image resolution. In the presence of large pressure differences, both the PPE method and the STE method generally benefit from the narrowed segmentation (denoted V−1 in the figure). In the range of moderate pressure differences (e.g., 10–20 mmHg), the most accurate results with the STE method were obtained on the reference segmentation, while the V−1 segmentation led to a slight overestimation. The accuracy of the PPE method was improved throughout the entire range of pressure differences. The dilated segmentation resulted in underestimating the pressure differences (V+1 values in Fig. 4). An important error of about 50 % occurs at the data point at 11 mmHg on the catheter axis, corresponding to the 40 % phantom at rest conditions. However, the catheter value is associated with a large amount of variability across measurement cycles, as indicated by the error bars, with $2\sigma = 5.7$ mmHg. The catheter value of the 60 % AoCo at rest, corresponding to the data point at 31 mmHg on the abscissa, also features a very high variability of $2\sigma = 11$ mmHg.

Fig. 5 summarizes the relative mismatch between the PPE and STE pressure difference estimates and catheter data in terms of the signed relative error $err_i = (y_i - z_i)/y_i$, with y_i and z_i denoting 4D Flow and catheter pressure differences, respectively. The data in the figure corresponds to the top row of Fig. 4, comparing the effect of the three segmentations, V+0, V−1 and V+1, for a voxel size of 0.9 mm, at the time of peak pressure difference. The relative mismatch with respect to the catheter results are consistently smaller with the STE method, except for the 50 % AoCo at rest, where the PPE method produces a more accurate match using the V+0 segmentation. In all cases, the manipulation of the segmentation had a much stronger impact on the PPE results. The normalized errors show an important disagreement of the catheter and 4D flow-derived pressure differences for the 40 % case at rest. Also the 40 %-stress data deviate significantly from the approximately linear trend of the 50 % and 60 % errors.

Tab. 2 quantifies the pressure difference mismatch and the sensitivity to the segmentation by means of the corresponding mean absolute relative errors. This metric indicates overall a significantly improved match of the STE method for all segmentations. The relative influence of the segmentation on the STE results is fairly small, slightly elevated only for the dilated V+1 segmentation. The mean error is slightly smaller using the standard segmentation V+0 than with V−1. The PPE method displays a much greater sensitivity to the segmentation. The most accurate fit is obtained using the reduced V−1 segmentation, while V+1

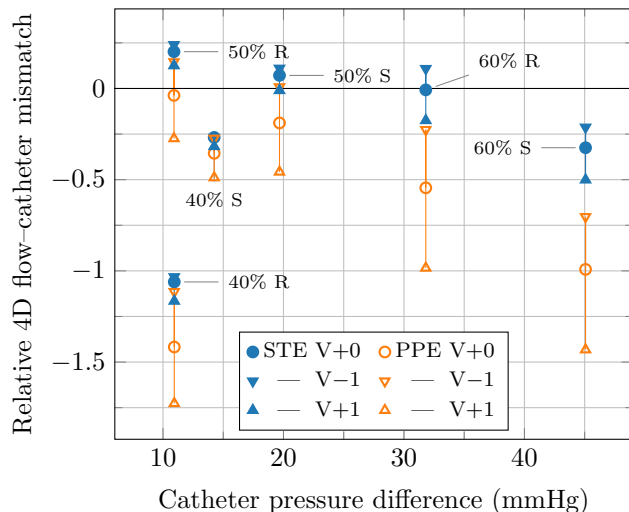


Figure 5: Relative peak mismatch of the STE and PPE methods with respect to catheter data, for default and dilated/reduced segmentations, plotted over the catheter pressure difference. Annotations indicate the AoCo severity and cardiac load (R: rest, S: stress). 4D Flow voxel size was 0.9 mm.

leads to errors more than twice as large.

Table 2: Mean absolute relative errors of STE and PPE peak pressure difference estimates with respect to catheter results over all AoCo phantom severities and flow conditions, for each of the segmentations V+0, V±1. 4D Flow data with voxel size 0.9 mm.

| | Segmentation: | V+0 | V-1 | V+1 |
|-------------------|---------------|------|------|------|
| Relative mismatch | PPE—catheter | 0.59 | 0.41 | 0.89 |
| | STE—catheter | 0.32 | 0.33 | 0.38 |

Time profiles of the pressure differences obtained with the V-1 segmentation (due to the greatly improved match of the PPE results with the catheter data) are shown in Figs. 6-8. Each figure contains the results of the PPE and the STE methods for 4D Flow resolutions of 0.9 mm (acquired) and 1.4 mm, 2.0 mm (subsampling from 0.9 mm) under rest and stress conditions and the averaged pressure differences from catheter measurements. The shaded areas indicate the band of two standard deviations σ over all measured cardiac cycles.

For the 40% AoCo phantom (Fig. 6), while showing a qualitatively correct behavior, the averaged catheter amplitude of the oscillation is generally underestimated by 3 mmHg to 7 mmHg with both methods under rest conditions. The variability of the catheter is large under rest conditions, and in the positive lobes, the 4D Flow results lie within the $\pm 2\sigma$ bounds.

The effect of the image resolution is weak. Under stress conditions, the peak pressure difference is recovered with a good accuracy. There is a negative

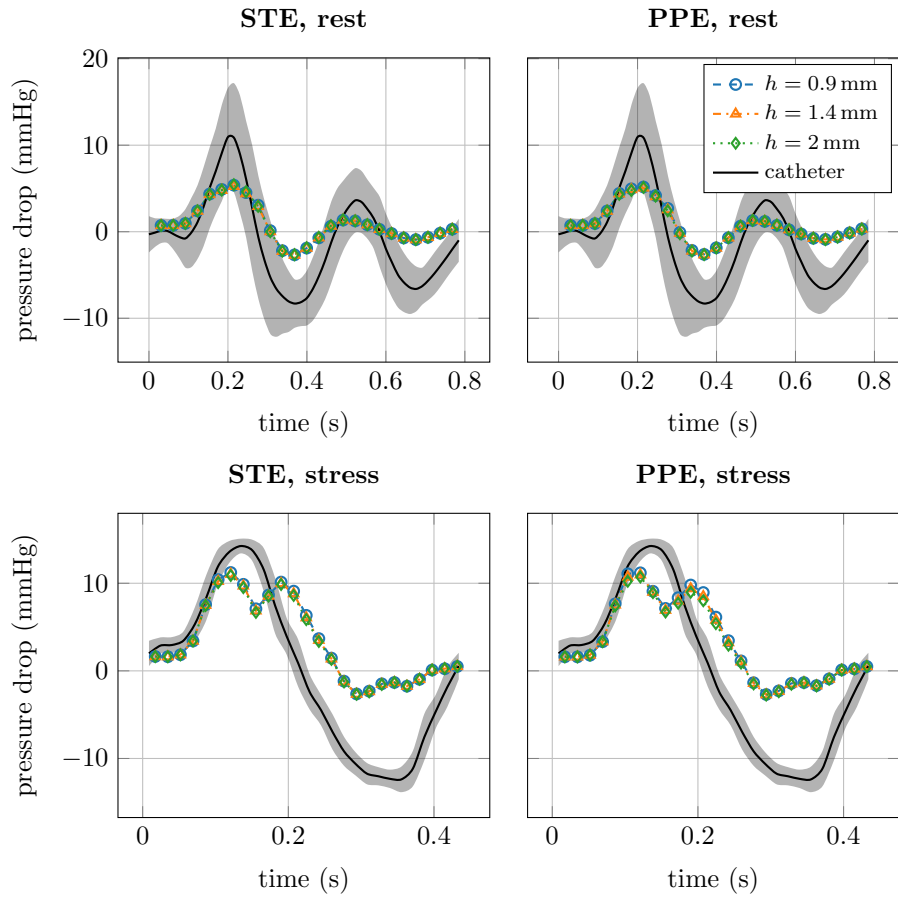


Figure 6: 40% AoCo phantom pressure differences obtained with STE (left column) and PPE (right column) under rest (first row) and stress conditions (second row) using voxel sizes of 0.9 mm, 1.4 mm, 2.0 mm compared to ground truth catheter data.

pressure difference lobe that was not correctly recovered by any of both methods. It must be noted that in the particular case of the 40 % AoCo phantom, artifacts appeared in the velocity measurements, most likely connected to issues with the experimental setup, like air bubbles. The 40 % AoCo phantom configuration was repeatedly scanned at different resolutions (results not reported) and the corresponding estimated pressure differences showed similar characteristics in all cases. The difference in the width of the systolic peak interval between the 4D Flow data and the catheter data is also likely to be caused by such issues with the experimental setup.

In the case of the 50 % AoCo phantom, the PPE method exhibits a very good quantitative agreement with the catheter results under rest conditions during the complete heart cycle, using the V-1 segmentation (Fig. 7). In comparison, the STE method overestimates the peak pressure difference. The STE result is improved by using the standard segmentation instead of the narrowed segmentation (cf. Fig. 4). Under stress conditions, similarly to the 40 % stress results, the 4D Flow-derived pressure differences show a double peak. The temporal duration of the peak appears to be overestimated.

Results from the 60 % AoCo phantom under rest conditions show an excellent agreement between the catheter data and the pressure difference computed with the STE method (Fig. 8). The PPE method underestimates the peak pressure difference. The discrepancy between the pressure difference reconstruction and catheter measurements increases for stress conditions. Both methods significantly underestimate the catheter pressure drop and yield flattened profiles around the peak location. Particularly the estimation of the PPE method severely deteriorates under the given flow conditions.

As a consequence of the larger linear system arising from the discretization of the STE equations by a factor of 4 compared to the PPE method, the STE method requires longer computational times and has a higher demand in RAM. Computation times for the 40 % AoCo phantom (25 velocity measurements) are listed in Tab. 3, for voxel sizes 0.9 mm and 2 mm. The most expensive computations with the STE method and high resolution data took about 4 minutes using direct linear solvers.

Table 3: CPU times of the pressure computation with the STE and the PPE methods from 25 time-resolved velocity measurements of the 40 % AoCo phantom.

| Method | Voxel size 2 mm | | Voxel size 0.9 mm | |
|--------|-----------------|--------|-------------------|-------|
| | Unknowns | Time | Unknowns | Time |
| PPE | 19 860 | 7.4 s | 223 072 | 35 s |
| STE | 79 440 | 14.9 s | 892 288 | 247 s |

4.2. Patient data

Pressure differences obtained by catheterization and from 4D Flow are shown in Fig. 9 for both patients. The locations where the pressure difference is evaluated is indicated by the green spheres in Fig. A.13 (right column). An excellent

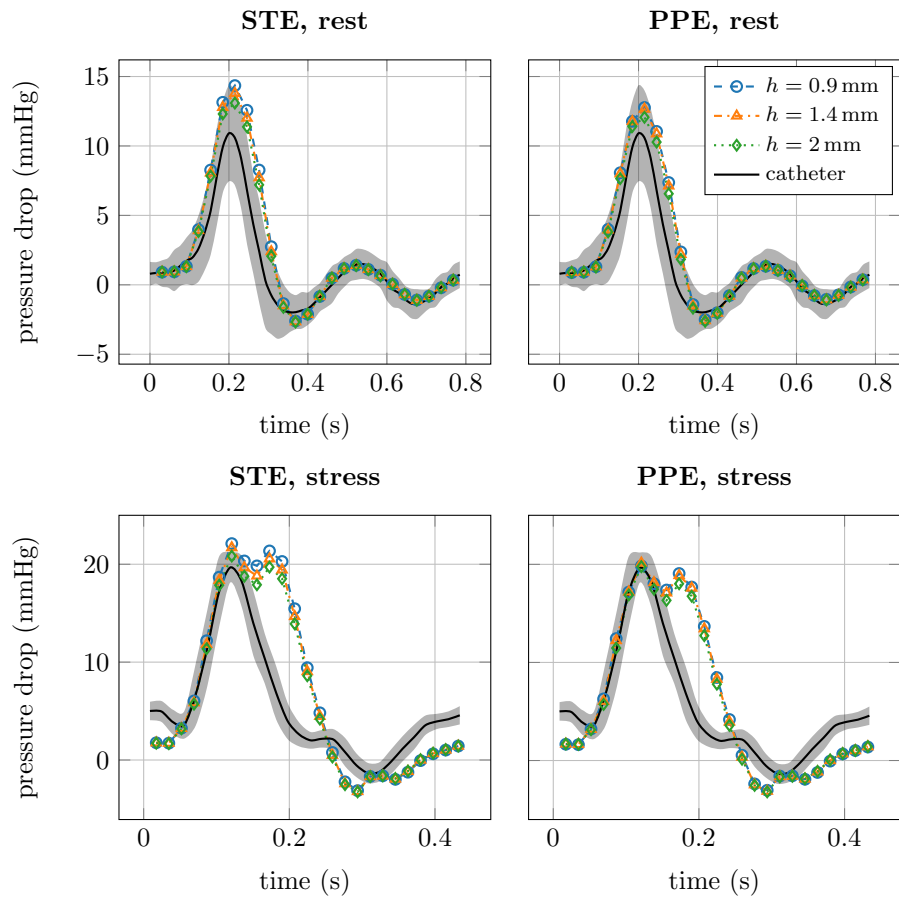


Figure 7: 50% AoCo phantom pressure differences obtained with STE (left column) and PPE (right column) under rest (first row) and stress conditions (second row) using voxel sizes of 0.9 mm, 1.4 mm, 2.0 mm compared to ground truth catheter data.

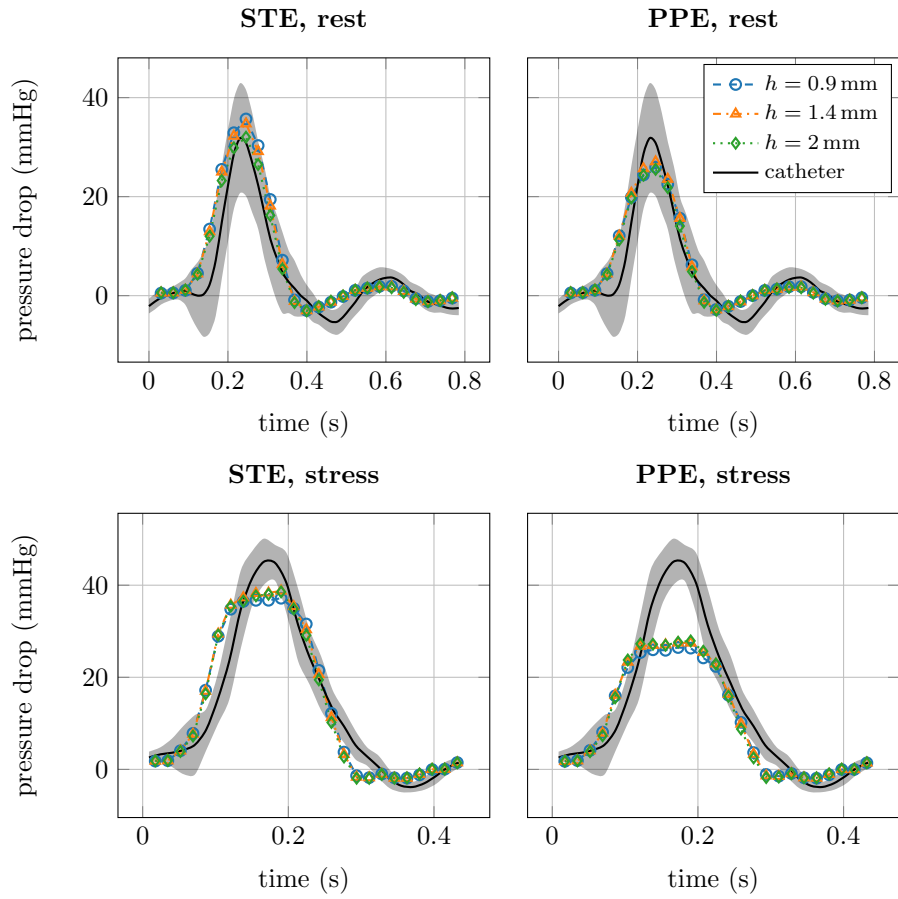


Figure 8: 60% AoCo phantom pressure differences obtained with STE (left column) and PPE (right column) under rest (first row) and stress conditions (second row) using voxel sizes of 0.9 mm, 1.4 mm, 2.0 mm compared to ground truth catheter data.

agreement of the STE pressure difference with catheter data was found for Subject 1 during systole. The local extrema after $t = 0.4$ s are underestimated. While similar qualitative agreement was found with the PPE method, it significantly underestimates the pressure difference during systole.

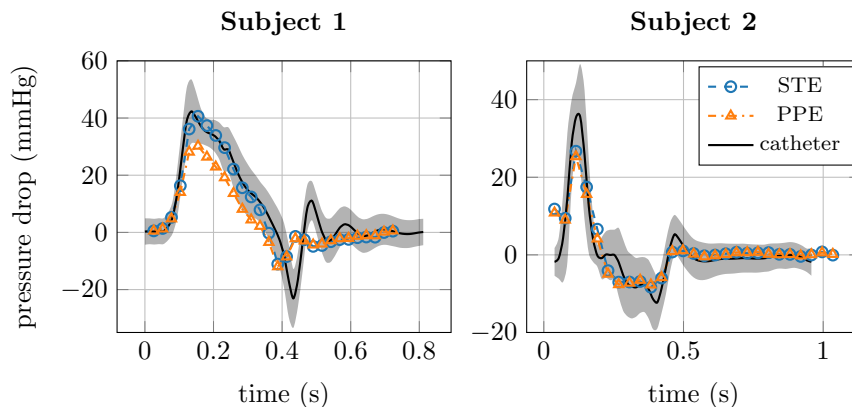


Figure 9: 4D Flow Pressure differences computed with STE and PPE compared to catheter data for Subject 1 and Subject 2.

Subject 2 exhibits good qualitative and quantitative agreement between catheter data and numerical pressure difference reconstruction. However, the pressure difference peak observed by catheterization is too steep to be captured by the time resolution of the 4D Flow protocol. The resulting maximum value lies below the catheter value, possibly because no velocity image was recorded matching exactly with the maximum pressure difference.

Note that the lengths of the cardiac cycles differ significantly between catheterization and MRI scans of both patients. This indicates a change in the heart rate which is likely to contribute to the differences between 4D flow and catheter pressure differences.

Reducing the diameter of the segmentation by one voxel was not possible in one of the patients due to the large voxel size with respect to the diameter. The original segmentations were thus not modified.

5. Discussion

Main findings. This study compared two relative pressure reconstruction methods for laminar flows, STE and PPE, in terms of accuracy and sensitivity with respect to image resolution, segmentation, AoCo severity and cardiac load (rest and stress).

The main finding of this study is that the STE method applied to 4D Flow data provides a significantly closer agreement with catheter measurements in terms of instantaneous pressure differences than the PPE method. The improvement in accuracy is most pronounced at large pressure differences (≥ 20 mmHg).

450
Image resolution & segmentation. Both methods are very robust with respect to the image resolution. While the effect of lower resolution data (larger voxel sizes) was to slightly reduce the pressure difference estimates, the magnitude of the effect did not have a significant impact on the quality of the results. The PPE results could be improved significantly in most cases by removing the outer layer of voxels at the vessel wall, and proved highly sensitive to the studied
455
 manipulation of the segmentation (i.e., comparing a high-fidelity segmentation with extensions or reductions by one layer of voxels at the walls). This is in line with [16] who also observed an improved accuracy of the PPE method by eliminating the outer layer of voxels. In contrast, the STE method appeared to be much more robust with respect to the segmentation, which had a relatively
460
 small influence on the results. In particular, the results are not always improved by choosing a heuristically manipulated segmentation, and the standard segmentation seems to be generally the best choice. The theory offers an explanation for the different sensitivities of the methods: the PPE method requires artificial (albeit consistent) boundary conditions for the pressure involving the near-wall
465
 velocities. These boundary values determine the solution in the interior, and errors due to partial-volume effects or low velocity-to-noise ratio (VNR) can contaminate the solution. The STE method completely avoids such pressure boundary conditions, which is likely the reason for the improved robustness.

470
 Dilated segmentations (V+1) add no-flow voxels with insignificant VNR, which introduce spurious information into the estimation problem. The pressure gradient computation is required to accommodate to such unphysical conditions, hence the deterioration of the results with both methods.

475
Regularity & turbulence. A further advantage of the STE method, guaranteed by the theory, is the fact that it searches the pressure in its *natural space*, while the PPE method imposes artificial higher regularity requirements, implying that its solutions are generally smoother than naturally required. Instead, the STE method allows for stronger spatial variations in the pressure and is capable of computing more realistic pressure fields. This fact is likely to cause the better agreement of the STE method with the catheter data, in relative and in absolute
480
 terms, in the regime of large pressure differences produced by the most severe 60% AoCo. Under such conditions, the flow is strongly convection-dominated, resulting in sharp gradients and large changes in the flow. These are precisely the flow features under which the PPE method must be expected to deteriorate due to the mentioned model assumptions.

485
 The significant underestimation by both methods in the most extreme scenario, the 60% AoCo under stress, warrants a closer look. It seems likely that in this case the flow periodically transitions to turbulence around systole and subsequently relaminarizes. No measurements of turbulent quantities have been made in this study to probe the presence of turbulent flow, and due to their
490
 inherently phase-averaged character, the 4D Flow data (Fig. A.12) do not allow deducing the presence of turbulences. We can merely note, that in the 60% AoCo phantom under stress conditions ($Re = 5000$), the flow field visibly deviates from the other scenarios (see Appendix A.2): no coherent flow structures

are visible, the vortices seem more broken and more chaotic. If turbulence is the
495 cause or noise, is indiscernible. Turbulent dissipation is known to be related to
pressure loss [36]. The marked failure of the STE and more so the PPE meth-
ods to recover the peak catheter pressure difference may be due to the omission
of the turbulence terms in (2) and, consequently, the effects of turbulent dis-
500 sipation. Under turbulent conditions, significant errors must be expected by
discarding the Reynolds' stress tensor in the flow model. It is reasonable to
assume that, if turbulence occurs, its effect on the pressure difference would be
much weaker in the less severe AoCo cases.

Special MRI sequences have been presented for the reconstruction of com-
ponents of the Reynolds' stress tensor [37], but require an increased scan times
505 (3 additional motion encoding acquisitions, more signal averages due to noise).
In spite of these limitations, some of the pressure difference estimation methods
have been extended to account for turbulence using the extended measurement
protocols. The PPE method including the Reynolds' stresses was assessed in [20]
under turbulent conditions. The term corresponding to the energy dissipated
510 by the Reynolds' stresses, i.e., the turbulent production, was introduced as a
stand-alone method in [38, 39] and was compared in numerical and experimental
phantoms with catheterization. In [40], the WERP and v WERP methods were
extended to include the Reynolds' stresses. Using the same phantom datasets
as in [39] it was confirmed that both methods improve their accuracy under
515 turbulent conditions when including the Reynolds' stresses. So far, no studies
have been reported extending the STE method to include turbulence effects.
Extending the STE method is straight forward, as for the PPE method, given
measurements of the Reynolds' stresses.

Future work should both study the possible occurrence of turbulence in the
520 present AoCo phantom, and the extension of the STE method to account for
turbulent effects.

High VENC. An additional factor is the very high VENC of 500 cm/s in the
60% AoCo under stress conditions. High VENC values cause uniformly high
noise levels which leads to low VNR in the regions of low flow velocities (i.e.,
525 outside of the jet core). In comparison to clinical 4D Flow with larger voxel
sizes, the high native resolution of 0.9 mm used in this studies leads to a lower
VNR, such that the present situation can be considered a "worst-case scenario"
regarding noise. The methods' sensitivity to noise remains a question for future
work. Dual-VENC techniques [41, 42, 43, 44], could alleviate the issue, allowing
530 for lower VENC-values (hence lower noise), but at increased scan times.

In-vivo results. The STE and the PPE pressure reconstruction methods were
also applied to real patient data. For one of the patients, the STE method
showed a great improvement over the PPE method. Both methods showed
satisfactory results for the second patient. From the findings in the phantom
535 experiments, the differences between PPE and STE in patient one is most likely
due to strong convective effects.

Limitations. A limitation of the study was the lack of availability of real low resolution MRI data for all scenarios, hence requiring synthetic subsampling of the high resolution data. Furthermore, only one segmentation was used for all cardiac phases. Another aspect to consider is the approach used for assessing the sensitivity to the segmentations, i.e., automatic manipulation instead of inter-operator variability. The latter was expected to be insignificant due to the excellent contrast and high SNR of the anatomic phantom images (see Fig. 1), hence an automatized voxel increment or decrement was adopted. Regarding the patient data, significant effects of inter-operator variability in the segmentation process are likely.

In addition, the comparison of catheter data with MRI scans is limited by the following observations. The locations where the catheter recorded the pressure during catheterization are only known approximately. A mismatch of the catheter positions with the locations selected for evaluating the computed pressure gradient can introduce significant errors. The pressure fields can be seen in Fig. 3 to vary near the extraction locations, both in the AAo and the DAo. The PPE and STE methods have the advantage, that the pressure difference can be evaluated in various locations, after inspection of the pressure field. Furthermore, the catheter measurements showed important variabilities among the cardiac cycles and their sampling rate and accuracy (~ 1 mmHg) were limited, which limits the authority of catheterization as ground truth in our study. Finally, representing an invasive technique, it is possible that the presence of the catheter in the vessel disturbs and alters the aortic flow during catheterization, while the 4D Flow data was acquired immediately after without the catheters. In the patient study it was seen that the heart rate changed significantly between catheterization and the MRI scan, hence possibly also affecting the outcome of this comparison.

6. Conclusion

In conclusion, in our phantom study, the STE method delivered results that were more accurate and robust with respect segmentation than the PPE method, in particular in severe cases of AoCo and under more challenging flow regimes. The effect of resolution was of minor importance. By heuristically eliminating the outermost layer of voxels of the segmentation, the PPE method could be significantly improved, but remains very sensitive to the segmentation. The STE method still provided a superior agreement with catheterization, without the need of artificially altering geometrically accurate segmentations.

The data will be made available upon request of the interested parties.

Acknowledgements

D.N. was supported by CONICYT grant 21151353. J.S. acknowledges funding by CONICYT-FONDECYT grant 3170737 and ANID-FONDECYT grant 11200481. A.O. was partially funded by ANID-FONDECYT grants 1191903 and

1201311, Basal Program CMM-AFB 170001 and FONDAP/15110009. A.O. and S.U. acknowledge funding from the Millennium Nucleus for Cardiovascular Magnetic Resonance. S.U. was also supported by FONDECYT grant 1181057. C.B. acknowledges funding from CONICYT Basal Program PFB-03 and from the European Research Council (ERC) under the European Unions Horizon 2020 research and innovation programme (grant 852544 – CardioZoom).

Conflict of interest

The authors declare no conflict of interest.

Appendix A. Description of measurement data

This section reviews the measurement data used in this study, see [17] and [24] for more details.

Appendix A.1. Catheterization data

The phase-averaged catheterization data obtained in the AAo and DAo locations is displayed in Fig. A.10 for the phantoms and in Fig. A.11 for the patients. The graphs include the catheter uncertainty across the measured cycles in terms of ± 2 standard deviation bands (shaded areas). The AAo pressure profiles are similar for all AoCo phantoms under the same cardiac load conditions. At rest, the peak amplitude slightly increases with increasing AoCo severity. Under stress conditions, it stands out that the 40% AoCo data has a higher minimum pressure than all other cases. The same case features a slight phase shift between the AAo and DAo signals. The DAo pressure visibly decreases in all cases with increasing severity. The catheter pressure variability across cycles also increases with AoCo severity. The spread is smaller under stress conditions.

The catheter pressures measured in the patients are shown in Fig. A.11. In contrast to the phantom data, marked phase shifts appear between the AAo and DAo pressures. This results in very large discrepancy between the instantaneous pressure differences as discussed here, and clinical peak-to-peak pressure differences, which only compare the difference between the overall maximum pressures. In Subject 2, the instantaneous pressure difference reaches 40 mmHg due to the phase shift, while the peak-to-peak pressure difference is close to 0 mmHg.

Appendix A.2. 4D Flow data

Peak velocity streamlines in the vicinity of the AoCo are shown in Fig. A.12 for all phantoms under rest and stress conditions. The displayed 4D Flow data correspond to the instant of maximum catheter pressure differences, see Figs. 6–8. Also included in the figures are iso-surfaces of the Q -criterion, commonly employed for identifying vortices [45, 46]. The levels of the iso-surfaces were adapted manually, such that the largest, dominant vortices were identifiable and fractional, cluttered regions minimized.

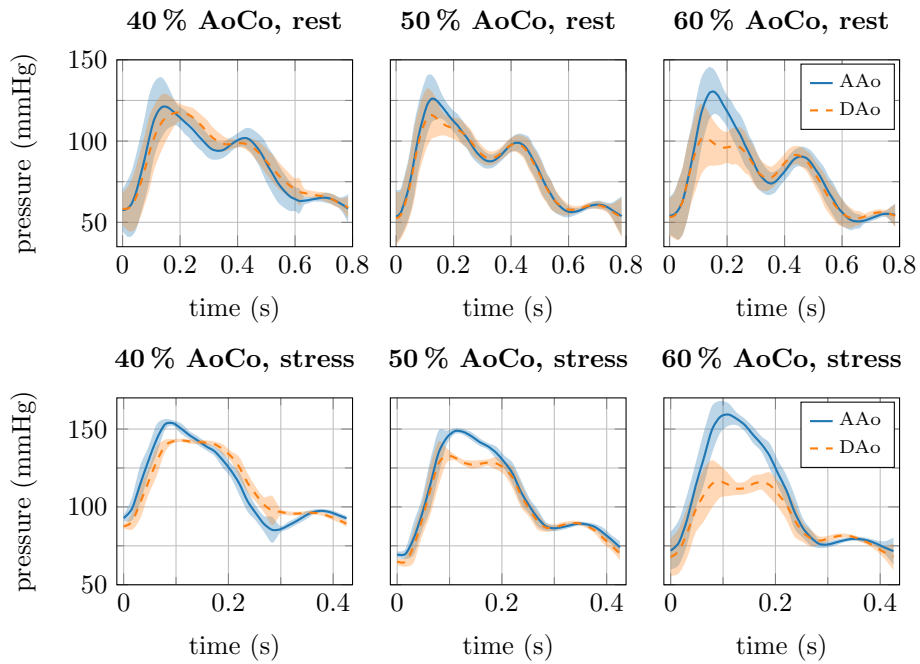


Figure A.10: Phantom catheter pressures measured in AAO and DAAo locations. The solid line indicates the phase-averaged pressure signals and the shaded area the ± 2 standard deviation bands.

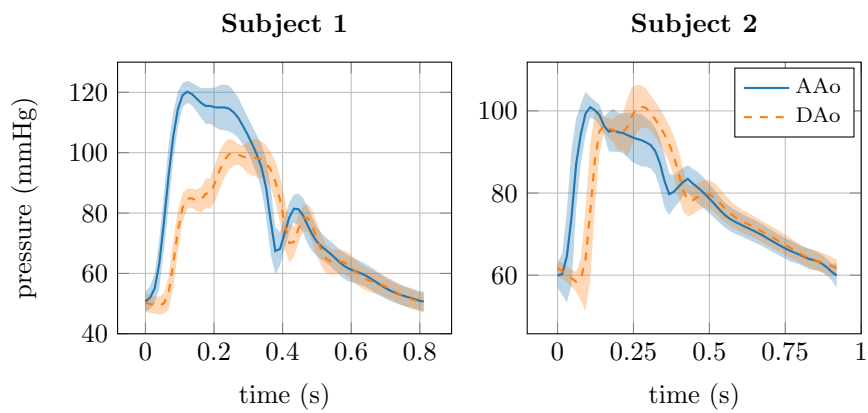


Figure A.11

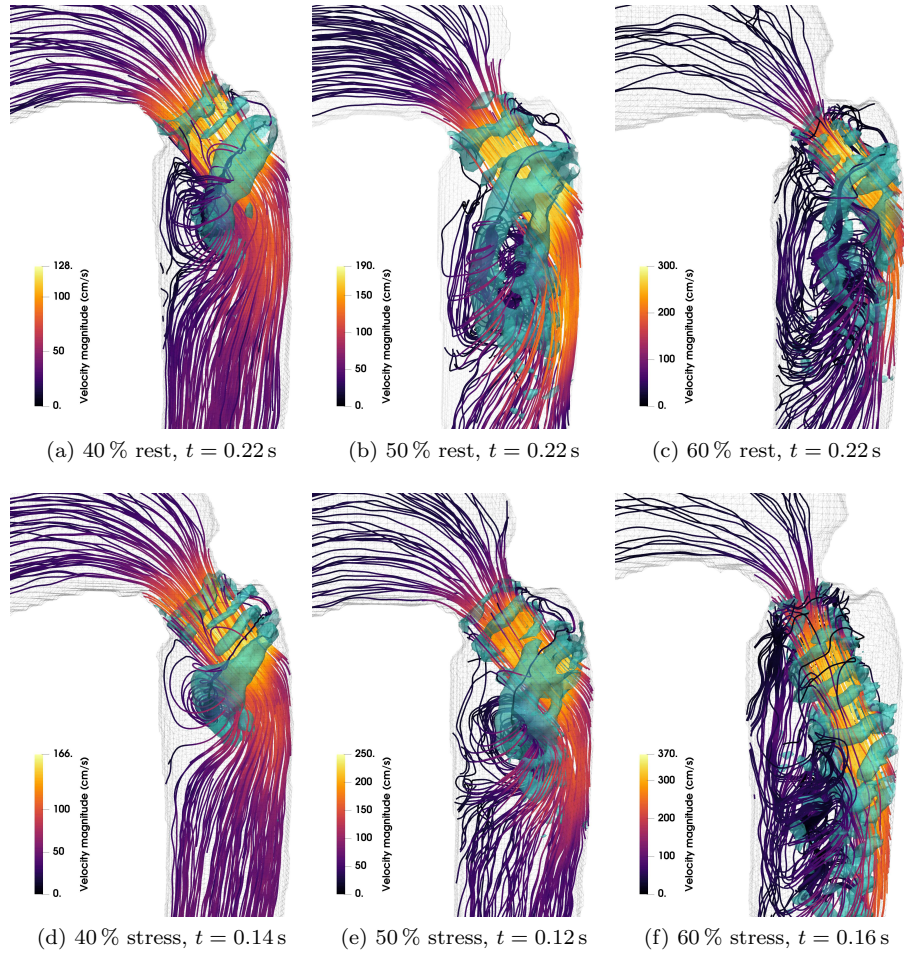


Figure A.12: Peak streamlines and selected Q -criterion iso-surfaces for vortex identification (green colors, different levels in all subfigures). Top row rest conditions: $Re \sim 3500$, bottom row stress conditions: $Re \sim 5000$. Times match the peak catheter pressure differences (cf. Figs. 6–8).

In all cases, the AoCo produces a strong jet impinging on the outer wall of the DAo. Strong recirculation zones, driven by the deflected flow, develop below the jets. Large vortex rings envelop the jets. For each severity, under stress conditions the maximum jet velocity is increased by 23 % to 30 % (at the time of the maximum catheter pressure difference).

In the 40 % AoCo phantom, the vortex ring associated with the large recirculation bubble is comparatively smooth and coherent. The flow quickly realigns and remains approximately parallel a short distance downstream of the recirculation zone. In comparison, the 50 % AoCo exhibits larger recirculation zones, both under the rest and stress conditions, and increasingly complex circulating flow patterns. The streamlines and Q -criterion iso-surfaces appear less smooth and coherent than in the 40 % case. For the 60 % AoCo, the recirculation zones are significantly larger with more chaotic and less coherently oriented streamlines. At rest, a large vortex, associated with the large contiguous Q -criterion ring structure, can be appreciated, superimposed by less orderly features. Under stress conditions, in Fig. A.12(f), a single large vortex cannot be identified, in contrast to all other scenarios. The Q -criterion iso-surface is significantly fractured, forming a number of tight vortex rings around the jet core. The streamlines in the recirculation zone are highly disorganized.

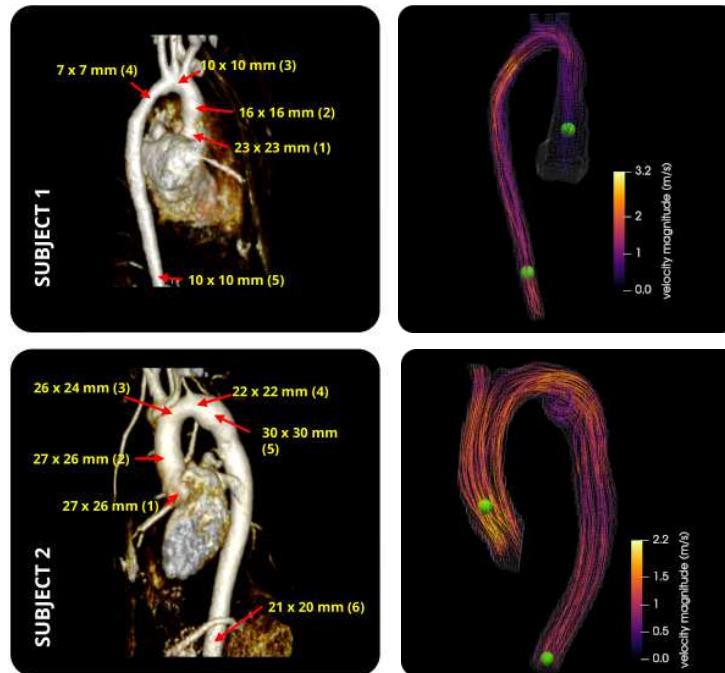


Figure A.13: Left column: angiographic images obtained using contrast agent, for both subjects, with annotations of the cross-sectional dimensions in terms of the widths in millimeters in two perpendicular directions. Right column: streamlines of 4D Flow at peak, spheres indicate locations of pressure difference calculation.

Fig. A.13 shows angiographic images of the patients paired with 4D Flow measurements corresponding to the peak systole. The flow appears to be highly regular, with high velocities in the narrow sections (positions (4)) and some recirculation in Subject 2 at position (5).

- 640 [1] R. Erbel, V. Aboyans, C. Boileau, E. Bossone, R. D. Bartolomeo, H. Eggebrecht, A. Evangelista, V. Falk, H. Frank, 2014 ESC Guidelines on the diagnosis and treatment of aortic diseases: Document covering acute and chronic aortic diseases of the thoracic and abdominal aorta of the adult. The Task Force for the Diagnosis and Treatment of Aortic Diseases of the European Society of Cardiology (ESC), *European heart journal* 35 (41) 645 (2014) 2873–2926.
- [2] C. A. Warnes, R. G. Williams, T. M. Bashore, J. S. Child, H. M. Connolly, J. A. Dearani, P. Del Nido, J. W. Fasules, T. P. Graham, Z. M. Hijazi, ACC/AHA 2008 Guidelines for the Management of Adults With Congenital Heart Disease: Executive Summary: A Report of the American College of Cardiology/American Heart Association Task Force on Practice Guidelines (Writing Committee to Develop Guidelines for the Management of Adults With Congenital Heart Disease) Developed in Collaboration With the American Society of Echocardiography, Heart Rhythm Society, International Society for Adult Congenital Heart Disease, Society for Cardiovascular Angiography and Interventions, and Society of Thoracic Surgeons, *Journal of the American College of Cardiology* 52 (23) (2008) 1890–1947. 650
- [3] T. F. Feltes, E. Bacha, R. H. Beekman III, J. P. Cheatham, J. A. Feinstein, A. S. Gomes, Z. M. Hijazi, F. F. Ing, M. De Moor, W. R. Morrow, Indications for cardiac catheterization and intervention in pediatric cardiac disease: A scientific statement from the American Heart Association, *Circulation* 123 (22) (2011) 2607–2652. 660
- [4] P. R. Hoskins, Accuracy of maximum velocity estimates made using Doppler ultrasound systems, *The British journal of radiology* 69 (818) 665 (1996) 172–177.
- [5] M. Markl, F. P. Chan, M. T. Alley, K. L. Wedding, M. T. Draney, C. J. Elkins, D. W. Parker, R. Wicker, C. A. Taylor, R. J. Herfkens, Time-resolved three-dimensional phase-contrast MRI, *Journal of Magnetic Resonance Imaging: An Official Journal of the International Society for Magnetic Resonance in Medicine* 17 (4) (2003) 499–506. 670
- [6] P. Dyverfeldt, M. Bissell, A. J. Barker, A. F. Bolger, C.-J. Carlhäll, T. Ebbers, C. J. Francios, A. Frydrychowicz, J. Geiger, D. Giese, M. D. Hope, P. J. Kilner, S. Kozerke, S. Myerson, S. Neubauer, O. Wieben, M. Markl, 4D flow cardiovascular magnetic resonance consensus statement, *Journal of Cardiovascular Magnetic Resonance* 17 (72). doi:10.1186/s12968-015-0174-5. 675

- [7] M. Markl, A. Frydrychowicz, S. Kozerke, M. Hope, O. Wieben, 4D flow MRI, *Journal of Magnetic Resonance Imaging* 36 (5) (2012) 1015–1036.
- [8] T. Ebbers, L. Wigstrom, A. F. Bolger, B. Wranne, M. Karlsson, Non-invasive measurement of time-varying three-dimensional relative pressure fields within the human heart, *Journal of biomechanical engineering* 124 (3) (2002) 288–293.
- [9] S. B. S. Krittian, P. Lamata, C. Michler, D. A. Nordsletten, J. Bock, C. P. Bradley, A. Pitcher, P. J. Kilner, M. Markl, N. P. Smith, A finite-element approach to the direct computation of relative cardiovascular pressure from time-resolved MR velocity data, *Medical Image Analysis* 16 (5) (2012) 1029–1037. doi:10.1016/j.media.2012.04.003.
- [10] C. Bertoglio, R. Nuñez, F. Galarce, D. Nordsletten, A. Osses, Relative pressure estimation from velocity measurements in blood flows: State-of-the-art and new approaches, *International Journal for Numerical Methods in Biomedical Engineering* 34 (2) (2018) e2925. doi:10.1002/cnm.2925.
- [11] H. Švihlová, J. Hron, J. Málek, K. R. Rajagopal, K. Rajagopal, Determination of pressure data from velocity data with a view toward its application in cardiovascular mechanics. Part 1. Theoretical considerations, *International Journal of Engineering Science* doi:10.1016/j.ijengsci.2015.11.002.
- [12] F. Donati, C. A. Figueroa, N. P. Smith, P. Lamata, D. A. Nordsletten, Non-invasive pressure difference estimation from PC-MRI using the work-energy equation, *Medical image analysis* 26 (1) (2015) 159–172.
- [13] D. Marlevi, B. Ruijsink, M. Balmus, D. Dillon-Murphy, D. Fovargue, K. Pushparajah, C. Bertoglio, M. Colarieti-Tosti, M. Larsson, P. Lamata, C. A. Figueroa, R. Razavi, D. A. Nordsletten, Estimation of Cardiovascular Relative Pressure Using Virtual Work-Energy, *Scientific Reports* 9 (1). doi:10.1038/s41598-018-37714-0.
- [14] F. Rengier, M. Delles, J. Eichhorn, Y.-J. Azad, H. von Tengg-Kobligk, J. Ley-Zaporozhan, R. Dillmann, H.-U. Kauczor, R. Unterhinninghofen, S. Ley, Noninvasive 4D pressure difference mapping derived from 4D flow MRI in patients with repaired aortic coarctation: Comparison with young healthy volunteers, *The international journal of cardiovascular imaging* 31 (4) (2015) 823–830.
- [15] E. Riesenkampff, J. F. Fernandes, S. Meier, L. Goubergrits, S. Kropf, S. Schubert, F. Berger, A. Hennemuth, T. Kuehne, Pressure fields by flow-sensitive, 4D, velocity-encoded CMR in patients with aortic coarctation, *JACC: Cardiovascular Imaging* 7 (9) (2014) 920–926.
- [16] L. Goubergrits, F. Hellmeier, D. Neumann, V. Mihalef, M. A. Gulsun, M. Chinali, A. Secinaro, K. Runte, S. Schubert, F. Berger, T. Kuehne,

- A. Hennemuth, M. Kelm, Patient-specific requirements and clinical validation of MRI-based pressure mapping: A two-center study in patients with aortic coarctation, *Journal of Magnetic Resonance Imaging* 49 (1) (2019) 81–89. doi:10.1002/jmri.26230.
- 720 [17] J. Urbina, J. A. Sotelo, D. Springmüller, C. Montalba, K. Letelier, C. Tejos, P. Irarrázaval, M. E. Andia, R. Razavi, I. Valverde, S. A. Uribe, Realistic aortic phantom to study hemodynamics using MRI and cardiac catheterization in normal and aortic coarctation conditions, *Journal of Magnetic Resonance Imaging* 44 (3) (2016) 683–697. doi:10.1002/jmri.25208.
- 725 [18] S. B. Pope, *Turbulent Flows*, Cambridge University Press, Cambridge ; New York, 2000.
- [19] J. Töger, M. J. Zahr, N. Aristokleous, K. M. Bloch, M. Carlsson, P.-O. Persson, Blood flow imaging by optimal matching of computational fluid dynamics to 4D-flow data, *Magnetic Resonance in Medicine* n/a (n/a). doi:10.1002/mrm.28269.
- 730 [20] H. Haraldsson, S. Kefayati, S. Ahn, P. Dyverfeldt, J. Lantz, M. Karlsson, G. Laub, T. Ebbers, D. Saloner, Assessment of Reynolds stress components and turbulent pressure loss using 4D flow MRI with extended motion encoding, *Magnetic resonance in medicine* 79 (4) (2018) 1962–1971.
- 735 [21] T. Ebbers, G. Farneback, Improving computation of cardiovascular relative pressure fields from velocity MRI, *Journal of Magnetic Resonance Imaging* 30 (1) (2009) 54–61.
- [22] M. E. Cayco, R. A. Nicolaides, Finite element technique for optimal pressure recovery from stream function formulation of viscous flows, *Mathematics of computation* 46 (174) (1986) 371–377.
- 740 [23] R. Temam, *Navier-Stokes Equations: Theory and Numerical Analysis*, Vol. 343, American Mathematical Soc., 2001.
- [24] C. Montalba, J. Urbina, J. Sotelo, M. E. Andia, C. Tejos, P. Irarrázaval, D. E. Hurtado, I. Valverde, S. Uribe, Variability of 4D flow parameters when subjected to changes in MRI acquisition parameters using a realistic thoracic aortic phantom, *Magnetic resonance in medicine* 79 (4) (2018) 1882–1892.
- 745 [25] J. Bock, A. Frydrychowicz, R. Lorenz, D. Hirtler, A. J. Barker, K. M. Johnson, R. Arnold, H. Burkhardt, J. Hennig, M. Markl, In vivo noninvasive 4D pressure difference mapping in the human aorta: Phantom comparison and application in healthy volunteers and patients, *Magnetic Resonance in Medicine* 66 (4) (2011) 1079–1088. doi:10.1002/mrm.22907.
- 750 [26] A. D. Holton, E. G. Walsh, B. C. Brott, R. Venugopalan, B. Hershey, Y. Ito, A. Shih, R. Koomullil, A. S. Anayiotos, Evaluation of in-stent stenosis

- 755 by magnetic resonance phase-velocity mapping in nickel-titanium stents,
Journal of Magnetic Resonance Imaging 22 (2) (2005) 248–257.
- [27] N.-S. Cheng, Formula for the viscosity of a glycerol- water mixture, Industrial & engineering chemistry research 47 (9) (2008) 3285–3288.
- [28] H. Luo, X. Fang, B. Ertas, Hilbert Transform and Its Engineering Applications, AIAA Journal 47 (4) (2009) 923–932. doi:10.2514/1.37649.
- 760 [29] J. A. Sotelo, I. Valverde, P. B. Beerbaum, G. F. Greil, T. Schaeffter, R. Razavi, D. E. Hurtado, S. Uribe, C. A. Figueroa, Pressure gradient prediction in aortic coarctation using a computational-fluid-dynamics model: Validation against invasive pressure catheterization at rest and pharmacological stress, Journal of Cardiovascular Magnetic Resonance 17 (S1). doi:10.1186/1532-429X-17-S1-Q78.
- 765 [30] R. Razavi, V. Muthurangu, S. R. Hegde, A. M. Taylor, MR-guided cardiac catheterization, in: Clinical Cardiac MRI, Springer, 2005, pp. 513–538.
- [31] P. Moore, MRI-guided congenital cardiac catheterization and intervention: The future?, Catheterization and cardiovascular interventions 66 (1) (2005) 1–8.
- 770 [32] J. Sotelo, J. Urbina, I. Valverde, C. Tejos, P. Irarrázaval, M. E. Andia, S. Uribe, D. E. Hurtado, 3D quantification of wall shear stress and oscillatory shear index using a finite-element method in 3D CINE PC-MRI data of the thoracic aorta, IEEE transactions on medical imaging 35 (6) (2016) 1475–1487.
- 775 [33] J. Sotelo, J. Urbina, I. Valverde, J. Mura, C. Tejos, P. Irarrazaval, M. E. Andia, D. E. Hurtado, S. Uribe, Three-dimensional quantification of vorticity and helicity from 3D cine PC-MRI using finite-element interpolations, Magnetic resonance in medicine 79 (1) (2018) 541–553.
- 780 [34] J. Bock, A. Frydrychowicz, A. F. Stalder, T. A. Bley, H. Burkhardt, J. Hennig, M. Markl, 4D phase contrast MRI at 3 T: Effect of standard and blood-pool contrast agents on SNR, PC-MRA, and blood flow visualization, Magnetic Resonance in Medicine: An Official Journal of the International Society for Magnetic Resonance in Medicine 63 (2) (2010) 330–338.
- 785 [35] M. Alnæs, J. Blechta, J. Hake, A. Johansson, B. Kehlet, A. Logg, C. Richardson, J. Ring, M. E. Rognes, G. N. Wells, The FEniCS Project Version 1.5, Archive of Numerical Software 3 (100). doi:10.11588/ans.2015.100.20553.
- 790 [36] P. Dyverfeldt, M. D. Hope, E. E. Tseng, D. Saloner, Magnetic resonance measurement of turbulent kinetic energy for the estimation of irreversible pressure loss in aortic stenosis, JACC: Cardiovascular Imaging 6 (1) (2013) 64–71.

- 795 [37] P. Dyverfeldt, A. Sigfridsson, J.-P. E. Kvitting, T. Ebbers, Quantification
of intravoxel velocity standard deviation and turbulence intensity by gener-
alizing phase-contrast MRI, *Magnetic Resonance in Medicine* 56 (4) (2006)
850–858. doi:10.1002/mrm.21022.
- [38] H. Ha, J. Lantz, M. Ziegler, B. Casas, M. Karlsson, P. Dyverfeldt,
800 T. Ebbers, Estimating the irreversible pressure drop across a stenosis by
quantifying turbulence production using 4D Flow MRI, *Scientific reports* 7
(2017) 46618.
- [39] H. Ha, J.-P. E. Kvitting, P. Dyverfeldt, T. Ebbers, Validation of pressure
drop assessment using 4D flow MRI-based turbulence production in various
shapes of aortic stenoses, *Magnetic Resonance in Medicine* 81 (2) (2019)
805 893–906. doi:10.1002/mrm.27437.
- [40] D. Marlevi, H. Ha, D. Dillon-Murphy, J. F. Fernandes, D. Fovargue,
M. Colarieti-Tosti, M. Larsson, P. Lamata, C. A. Figueroa, T. Ebbers,
et al., Non-invasive estimation of relative pressure in turbulent flow using
virtual work-energy, *Medical Image Analysis* 60 (2020) 101627.
- 810 [41] E. Nett, K. Johnson, A. Frydrychowicz, A. Muñoz, E. Schrauben, C. Fran-
cois, O. Wieben, Four-dimensional phase contrast mri with accelerated dual
velocity encoding, *Journal of Magnetic Resonance Imaging* 35 (6) (2012)
1462–1471.
- [42] H. Ha, G. B. Kim, J. Kweon, Y.-H. Kim, N. Kim, D. H. Yang, S. J. Lee,
815 Multi-venv acquisition of four-dimensional phase-contrast mri to improve
precision of velocity field measurement, *Magnetic resonance in medicine*
75 (5) (2016) 1909–1919.
- [43] F. Callaghan, R. Kozor, A. Sherrah, M. Valley, D. Celermajer, G. Figtree,
S. Grieve, Use of multi-velocity encoding 4d flow mri to improve quantifica-
820 tion of flow patterns in the aorta, *Journal of Magnetic Resonance Imaging*
43 (2) (2016) 352–363.
- [44] H. Carrillo, A. Osses, S. Uribe, C. Bertoglio, Optimal Dual-VENC (ODV)
Unwrapping in Phase-Contrast MRI, *IEEE Transactions on Medical Imag-*
ing (2018) 1–1doi:10.1109/TMI.2018.2882553.
- 825 [45] G. Haller, An objective definition of a vortex, *Journal of fluid mechanics*
525 (2005) 1.
- [46] Y. Dubief †, F. Delcayre ‡, On coherent-vortex identification in turbulence,
Journal of Turbulence 1 (2000) N11. doi:10.1088/1468-5248/1/1/011.